

pubs.acs.org/JPCL Letter

Octahedral Distortions Generate a Thermally Activated Phonon-Assisted Radiative Recombination Pathway in Cubic CsPbBr₃ Perovskite Quantum Dots

Vivien L. Cherrette, Finn Babbe, Jason K. Cooper,* and Jin Z. Zhang*



Cite This: J. Phys. Chem. Lett. 2023, 14, 8717–8725



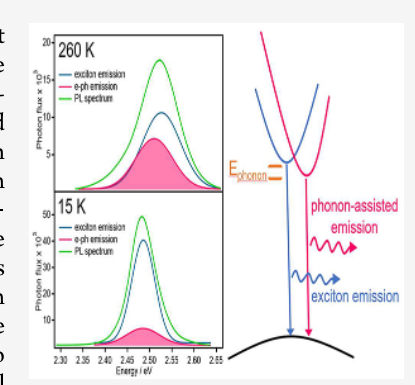
ACCESS I

III Metrics & More

Article Recommendations

Supporting Information

ABSTRACT: Exciton—phonon interactions elucidate structure—function relationships that aid in the control of color purity and carrier diffusion, which is necessary for the performance-driven design of solid-state optical emitters. Temperature-dependent steady-state photoluminescence (PL) and time-resolved PL (TRPL) reveal that thermally activated exciton—phonon interactions originate from structural distortions related to vibrations in cubic CsPbBr₃ perovskite quantum dots (PQDs) at room temperature. Exciton—phonon interactions cause performance-degrading PL line width broadening and slower electron—hole recombination. Structural distortions in cubic PQDs at room temperature exist as the bending and stretching of the PbBr₆ octahedra subunit. The PbBr₆ octahedral distortions cause symmetry breaking, resulting in thermally activated longitudinal optical (LO) phonon coupling to the photoexcited electron—hole pair that manifests as inhomogeneous PL line width broadening. At cryogenic temperatures, the line width broadening is minimized due to a decrease in phonon-assisted recombination through shallow traps. A fundamental understanding of these intrinsic exciton—phonon interactions gives insight into the polymorphic nature of the cubic phase and the origins of performance degradation in POI



polymorphic nature of the cubic phase and the origins of performance degradation in PQD optical emitters.

ll-inorganic CsPbBr₃ perovskite quantum dots (PQDs) Aare a class of solution-processable semiconductor nanocrystals that have gained significant attention for solid-state lighting and photonics applications due to their facile and lowcost fabrication, tunable optical properties, and near-unity photoluminescence (PL) quantum yields (QY) (>90%). 1-5 Although very promising, PQDs lack in performance in comparison to more mature semiconductor quantum dots (QDs), e.g., II-VI QDs which have narrow emission line widths and, therefore, are very color pure. PQDs typically have emission line widths ranging from 70 to 120 meV at room temperature, while colloidal II-VI QD emission line widths range between 20 and 60 meV.6 Narrow emission is desired for solid-state light-emitting devices and QD displays. We therefore seek to understand the fundamental origins of line width broadening in the PL spectrum of PQDs. PL line width broadening can originate from several known phenomena, including defects, phase impurities, and exciton-phonon

Structural defects in the core and on the nanocrystalline surface of QDs bring about inhomogeneous line width broadening and reduced PL QY efficiency. The PL line width broadening can arise from the development of trap states within the bandgap that create low-energy emission sidebands. Deep trap states, localized near the middle of the bandgap, generate nonradiative recombination pathways that can significantly reduce PL QY due to multiphonon emission. 9

PQDs are more defect tolerant in comparison to typical semiconductor QDs, allowing them to reach relatively high PL QY efficiencies (\sim 70–80%) with low cost and simple synthetic methods. 10 Perovskite defect tolerance is attributed to the large formation energies of vacancies and antisites that cause deep trap states and diminishing PL QY.11 However, defect formation in PQDs is drastically different from their corresponding bulk materials primarily due to their large surface-to-volume ratio. The substantial number of uncoordinated surface atoms/ions compared to core atoms/ions often makes surface recombination a primary PL QY loss mechanism. High-quality synthesis methods are necessary to achieve near-unity PL QYs (>90%) and suppress nonradiative recombination. The chemical environment, storage conditions, and solution temperature can shift the equilibrium away from the ligand passivated surfaces exposing surface defects and causing PL quenching. Incomplete surface passivation can also introduce defects that would contribute to PL line width broadening despite achieving relatively high PL QY efficiency. 12,1

Received: September 12, 2023 Accepted: September 15, 2023 Published: September 22, 2023





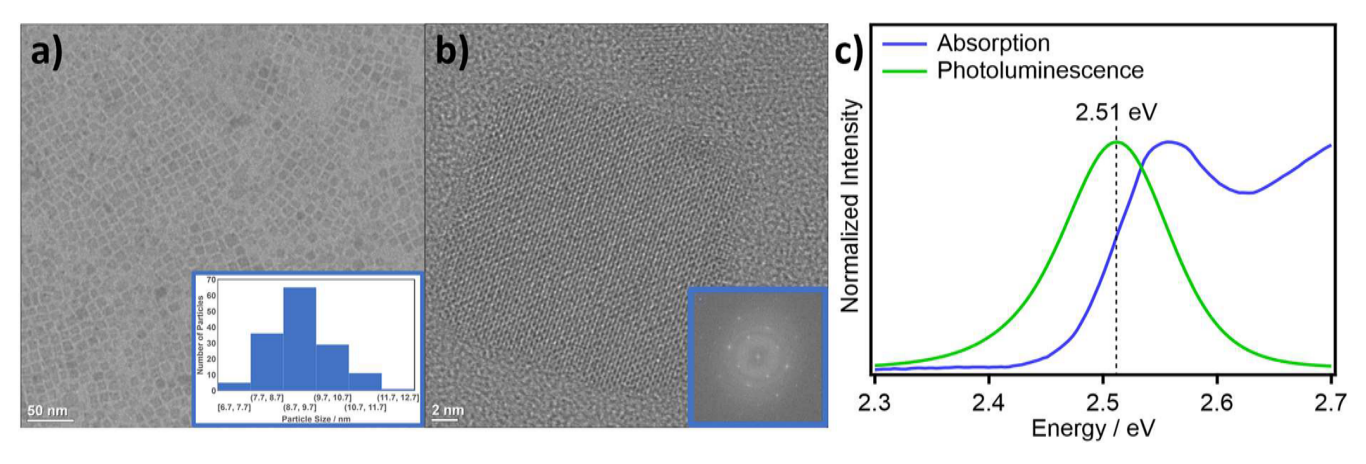


Figure 1. (a) HR-TEM of PQDs illustrating monodispersed particle size histogram (inset), (b) HR-TEM of single PQD showing cubic crystallinity and fast Fourier transform (FFT) (inset), and (c) CsPbBr₃ PQD PL and absorption spectrum overlaid and normalized to the corresponding peaks.

Inhomogeneous PL line width broadening can also arise from impurity crystalline phases. The ABX₃ perovskite structure (A= Cs⁺, methylammonium (MA⁺), formamidinium (FA⁺); B= Sn²⁺, Pb²⁺; $X = Cl^-$, Br⁻, I^-) consists of a 3D corner-sharing [BX₆]⁴⁻ octahedral framework with A cations centrally coordinated between. Bulk CsPbBr3 perovskites form monoclinic, orthorhombic, or tetragonal crystalline phases at low temperatures (T < 361 K), while the cubic phase exists at high temperatures (T > 403 K). ¹⁴ In contrast, nanocrystals can be stabilized at room temperature in target crystal phases. 1 For example, the room-temperature CsPbBr₃ nanocrystals were first reported as cubic (Pm3m), 10 but reports of tetragonal $(P4/mbm)^{16}$ and orthorhombic $(Pbnm \text{ or } Pnma)^{1}$ phases followed. As each crystal phase has different optoelectronic properties, inhomogeneous PL broadening can result from impurity phases. Yet, even for seemingly high phase-pure nanocrystal, some phase impurities may exist as thermally activated structural distortions known as polymorphous networks. 14,18

Polymorphous networks that arise from the thermal disorder of the lattice can also alter the optical properties. These networks are characterized as the breaking of local symmetry by tilting, rotations, and B-cation displacement. The most common polymorphic network in CsPbBr₃ is rigid rotations of the PbBr₆ octahedral cages, commonly called octahedral tilting. This octahedral distortion breaks the cubic symmetry and can alter the energetics of the band structure. Additionally, octahedral distortions have been known to induce exciton—phonon coupling that causes low-energy PL line width broadening and slower PL lifetimes. 21–24

Exciton—phonon interactions can cause line width broadening by introducing vibrational relaxation pathways for photoexcited carriers causing phonon-assisted recombination. Longitudinal optical (LO) phonons can only exist in rotationally distorted perovskites, like tetrahedral and orthorhombic, and not in the rigid, monomorphous cubic structures. As such, LO-phonon—exciton coupling will emerge in the systems containing octahedral distortions. An examination of the relationship between lattice distortions and exciton—phonon coupling will help gain insight into the structure—function relationships that play a detrimental role in the PL properties.

The monomorphous cubic phase PQDs should have the best color purity compared to other low-symmetry phases due to the lack of structural distortions that can cause PL line width broadening.^{22,225} However, recent studies reveal the accepted monomorphous cubic structure may also undergo polymorphous distortions.¹⁴ To elucidate the true nature of the cubic structure and the origin of PL line width broadening, it is necessary to understand exciton—phonon coupling in the PL spectrum.

As phonons are thermally activated, the effects of phonon-assisted recombination pathways are typically studied by low-temperature PL and TRPL. However, temperature-dependent phase transitions make studying exciton—phonon coupling at low temperature impossible. As mentioned, the temperature dependence of the crystal phases in bulk CsPbBr3 is well recognized: cubic (T > 403 K), tetragonal (403 K > T > 361 K), and orthorhombic (T < 361 K). However, temperature exciton—phonon coupling in the cubic phase we have utilized a nanocrystalline system in which the cubic phase is captured during high-temperature synthesis and stabilized over all temperature ranges through the use of surface ligands. However, temperature is surface ligands.

In this work, homogeneous cubic PQD nanocrystals were synthesized with near-unity PL QY (>90%). We examined these particles by temperature-dependent PL studies between 15 and 295 K to investigate the relationship between exciton—phonon interactions and structural distortions. We found that cubic PQDs experience polymorphous distortions at room temperature despite being in the pure cubic phase. These distortions cause symmetry breaking that results in thermally activated phonon coupling to the photoexcited exciton that manifests as inhomogeneous PL line width broadening. At low temperatures, the inhomogeneous broadening is eliminated due to reduced octahedral distortions related to vibration.

Following the well-known hot-injection method, CsPbBr₃ PQDs were synthesized at 443 K to form the high-temperature cubic phase. 10 High-resolution transmission electron microscopy (HR-TEM) data in Figure 1a confirm monodisperse PQDs that are 9.3 \pm 0.9 nm in length. Figure 1a inset shows the particle size distribution collected from 150 particles. Figure 1b shows the cubic phase of the single nanocrystal with 4.1 Å d-spacing and the Fourier transform diffraction pattern in the inset. 17,33

The optical properties of the PQDs were measured in a tetradecane suspension. Since aggregation of PQDs can spontaneously occur at lower temperatures and quench PL emission, high freezing point suspension solvents are necessary for low-temperature experiments. The tetradecane freezing point is 278.5 K, which is effective at eliminating PQD

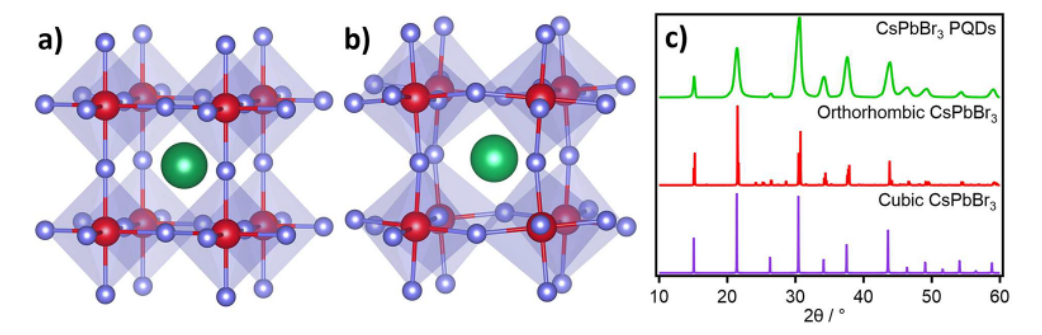


Figure 2. (a) Cubic phase perovskite unit cell where the central Cs $^+$ cation (green) is caged between a corner-sharing [PbBr $_6$] $^{-4}$ octahedral framework (Pb $^{2+}$, red/Br $^-$, purple), (b) orthorhombic phase (not entire unit cell) used to display octahedral tilting of the PbBr $_6$ octahedral cages, and (c) XRD spectrum of PQDs (green) showing cubic phase and high crystallinity at room temperature. Theoretical powder XRD patterns for cubic and orthorhombic structures were calculated in VESTA [COD ID: 1533063 (cubic) and 4510745 (orthorhombic)]. Reference pertains to data and not the figure itself.

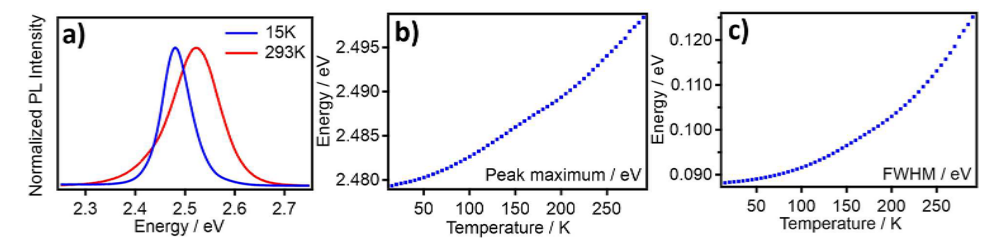


Figure 3. (a) Normalized temperature-dependent steady-state PL measured at 15 and 293 K. PL measurements were taken using a 405 nm pulsed laser and 1800 lines/mm grating for direct comparison to the TRPL. The temperature-dependent PL trend analysis of (b) peak position (eV) and (c) full-width half-maximum (fwhm) (eV). PL trend measurements were taken using a 405 nm continuous wave laser. PL measurements were conducted after allowing the sample to thermally equilibrate in the dark for 15 min. A 150 lines/mm grating was used to complete the trend analysis.

aggregation and preserving the PL QY at low temperatures. Figure 1c shows the absorption and PL spectra at room temperature (293 K). The free exciton absorption energy is 2.56 eV, and the PL maximum is at 2.51 eV, indicating a Stoke's shift of 0.05 eV. This binding energy agrees well with previous reports ranging from 38 to 58 meV. 34,35 Concentration and power-dependent studies were conducted to ensure nonlinear effects, such as photon recycling, did not play an extended role on PL line width broadening as previous reports have found. Figures S1 and S2 in the Supporting Information show that concentration and excitation intensities were well within the linear regime and play a negligible role in the PL line width broadening.

The PL spectrum has a full-width half-maximum (fwhm) of 110 meV thus showing comparably small spectral broadening on par with previous PQD reports. Fitting of the PL spectrum in Figure S3 reveals broadening, causing red tailing in the emission spectrum; Table S1 provides the Gaussian fit parameters. Two peaks were identified at 2.514 eV, corresponding to the exciton emission, and 2.499 eV, corresponding to the broadening component. The low-energy broadening could arise from a variety of PQD properties, including defects, crystal phase impurities, and exciton—phonon interactions. We hypothesize that the low-energy tailing in the emission spectrum is caused by exciton—phonon coupling due to octahedral distortions at room temperature. However, the following experiments were done to rule out broadening caused by defects and crystal phase impurities.

Deep surface defects often reduce PL QY and result in lowenergy sidebands that cause inhomogeneous PL line width broadening.^{37–39} Therefore, to deconvolve phonon interactions in the PL, deep defects in PQDs must be negligible. PL QY was calculated using relative methods and compared against perylene dye. The PQDs consistently exhibit PL QY of 91% and are stable for more than 1 month under an inert atmosphere with no signs of degradation. Table S2 shows the longevity of the PL QYs of the particles in different storage conditions; storing particles under $\rm N_2$ gas is the most effective. This near-unity PL QY efficiency suggests that the PQDs have excellent surface passivation and minimal deep defects. Therefore, deep defect-assisted radiative and nonradiative emission pathways are negligible, ensuring efficient charge carrier generation and recombination. 40,41

Perovskite nanocrystal syntheses have been known to produce both orthorhombic and cubic phases. ^{10,17,25,43} To determine the crystallinity and crystal phase of the PQDs, we utilized HR-TEM, X-ray diffraction (XRD), and Raman spectroscopy.

The cubic and orthorhombic phases of CsPbBr₃ are illustrated in Figure 2a,b, where the central Cs⁺ cation (green) is caged between a corner-sharing [PbBr₆]⁻⁴ octahedral framework (Pb²⁺, red/Br⁻, purple). The full orthorhombic unit cell was not used to display octahedral tilting of the PbBr₆ octahedral cages. Figure 1b shows the room-temperature HR-TEM image of a single nanocrystal with cubic symmetry. The measured 4.1 Å *d*-spacing is in agreement with the expected value 4.15 Å from the {110} cubic plane of the cubic crystal. Additionally, 3.0 Å *d*-spacing was also observed in good agreement with the expected 2.94 Å of the {200} cubic plane.

The XRD data in Figure 2c agree with cubic symmetry PQDs. However, assigning the crystal phase based only on

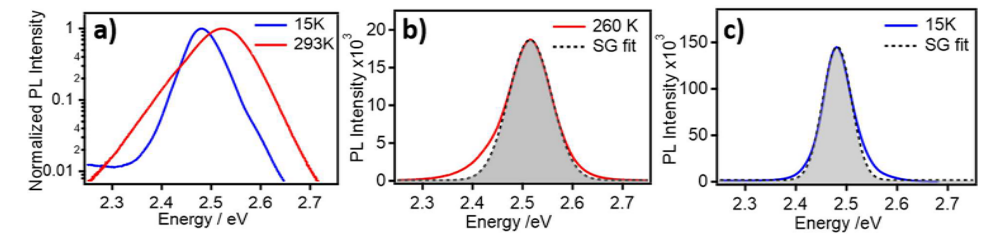


Figure 4. (a) Normalized steady-state PL spectra plotted semilogarithmically show low-energy red tail and possible phonon coupling mode. (b) 260 K PL fit with single Gaussian (SG). (c) 15 K PL fit with SG. PL measurements were conducted under the same conditions as in Figure 3a.

XRD is challenging due to similar diffraction patterns of the two phases. As such, we employed room-temperature Raman scattering to confirm the cubic phase crystals. Orthorhombic and tetragonal structures produce a sharp peak at approximately 105 cm⁻¹, which is absent from the pristine cubic structures. As seen in Figure S4, the PQDs exhibit no significant sharp features, and all peaks are attributed to tetradecane solvent. This is typical of perovskite crystals with cubic phase symmetry, as they do not have Raman active modes. 44

We use temperature-dependent PL to evaluate the role of exciton—phonon coupling on the PL line width broadening. However, temperature-dependent phase transitions occur in perovskite bulk material contributing to PL line width broadening. As demonstrated in previous studies, the PQD's 0D nanocrystalline surface should stabilize the crystal phase well below the phase transition temperatures expected in the bulk systems. 15 Low-temperature PL experiments were conducted to ensure that the crystalline phase remains unchanged for the sole examination of intrinsic excitonphonon interactions. Temperature-dependent steady-state PL in Figure 3a reveals a blue shift (shift to higher energy) with increasing temperature. The peak shifts from 2.48 eV (15 K) to 2.52 eV (293 K), which indicates the band gap widens with increasing temperature which is consistent with other reports of perovskite materials. 32,37,44 This is atypical of most semiconductors (Si, III-V, II-VI, etc.) that display a red shift, or band gap narrowing, with increasing temperatures due to lattice vibrations that increase the interatomic distance.⁴⁵ In PQDs the widening is attributed to the combination of lattice expansion and octahedral tilting.²⁰

Lattice expansion and octahedral tilting influence the CsPbBr₃ electronic energy levels, because of the orbital overlap in the bands. The valence band maximum (VBM) is composed of hybridized antibonding Pb 6s and Br 5p orbitals. ^{20,46} Lattice expansion and octahedral tilting decrease the Pb—Br overlap which stabilizes the VBM, thus lowering the band energy. The conduction band maximum (CBM) is composed of Pb 6p nonbonding orbitals. As such, the CBM is less affected by changes in the orbital overlap. The combined effect is a widening of the bandgap at increasing temperature.

Figure 3b shows a gradual shift of the PL peak maximum from 2.48 eV at 15 K to 2.50 eV at 290 K. The gradual progression is characteristic of PQDs, while bulk material temperature-dependent behavior shows stepwise discontinuities at the phase transition temperatures. The lack of such discontinuities indicates no evidence for first-order phase transitions, suggesting the cubic crystal phase is retained from 15 to 290 K. The retention of cubic crystal symmetry suggests the room-temperature PL line width broadening is likely due to exciton—phonon interactions intrinsic to the cubic structure.

The temperature-dependent PL line width trend gives insight into exciton—phonon interactions. Figure 3c shows a gradual increase of the line width from 88 meV at 15 K to 125 meV at 290 K. Spectral broadening has a combination of homogeneous and inhomogeneous components. Homogeneous broadening at elevated temperature is due to lattice vibrations and has been demonstrated in a variety of solid-state semiconductors, including CsPbBr₃ bulk, single crystals, and other nanocrystal counterparts. Defende the decrease in PL line width broadening at 15 K is partly from reducing lattice vibrations. However, we attribute the inhomogeneous component, manifested as red (low-energy) tailing at room temperature, to exciton—phonon coupling that brings about a phonon-assisted emission pathway.

Exciton—phonon coupling is thermally activated and close in energy to the exciton manifesting inhomogeneous broadening or low-energy tailing. Low-temperature PL studies were further analyzed to observe inhomogeneous broadening from phonon-assisted emission. Figure 4a displays a semilogarithmic plot of the PL spectral profile at 15 and 293 K to better express the temperature-dependence of the low-energy tailing. The room-temperature tailing is shown by a non-Gaussian low-energy shoulder that diminishes at 15 K. The shoulder is not discrete, supporting that the low-energy tailing is close in energy to the exciton emission. Furthermore, both measurements were fit with a single Gaussian (SG) fit function, displayed in Figures 4b,c. The shaded SG fits show the disappearance of the low-energy tailing at 15 K. The gradual disappearance of the low-energy tailing is also seen at 130 and 170 K in Figure S5.

Previous literature reports the opposite for perovskite nanocrystals in terms of low-energy tailing or even the appearance of a discrete peak at low temperatures. ^{22,25,37,48} The peak at low temperatures is attributed to carriers recombining through a phonon-assisted emission pathway. Iaru et al. found similar phonon-assisted emission in orthorhombic crystal phase PQDs due to locked structural distortions. ²² The low-energy tailing occurs only at elevated temperatures and is largely mitigated at 8 K. This suggests that the phonon-assisted emission pathway is due to thermally induced structural distortions. TRPL kinetics studies are needed to confirm the presence of the two emission pathways at room temperature: (1) exciton recombination and (2) phonon-assisted recombination.

In efforts to resolve the thermally activated phonon-assisted emission pathway, TRPL was utilized to verify the presence of multiple radiative recombination pathways buried within the PL spectrum. Figure 5 depicts TRPL behavior at 15 and 295 K. At 295 K, the PL decay time was best fit using a double exponential (DE) function. The 15 K had best fit agreement with a single exponential (SE) function. The biexponential character at room temperature verified the presence of two

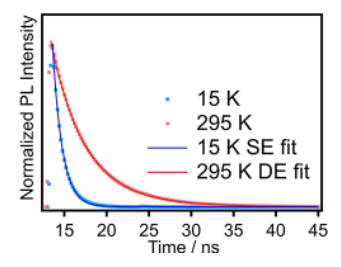


Figure 5. Time-resolved PL at 15 K (raw data, blue dots, and single exponential (SE) fit, blue line) and 295 K (raw data, red dots, and double exponential (DE) fit, red line). TRPL measurements were conducted under the same conditions as in Figure 3a.

emission pathways, while the more single exponential character at 15 K verified the presence of one dominant emission pathway. The disappearance of one emission pathway at 15 K suggests that there is indeed a thermally activated emission pathway generated at room temperature.

Further resolution of the discrete energy levels of the exciton emission and the alternate thermally activated emission pathways is necessary to reveal an exciton-phonon coupling mode that can be structurally assigned. Energy-dependent TRPL experiments at 15 and 260 K displayed in Figure 6 were conducted to resolve the discrete energies of multiple emission pathways. These experiments were carried out by measuring the TRPL at several monochromator wavelengths. The exponential decays at 260 K in Figure 6a were best fit with PL decay times held constant at 2.1 and 4.1 ns. These PL decay times are consistent with PL lifetimes previously observed in the literature.⁴⁹ After fitting the respective PL exponential decay amplitudes, the presence of two energy states at 260 K, 2.5119 and 2.5282 eV, were resolved. The sum of these energy states was overlaid (yellow) with the steadystate PL spectrum (green dashed line) to confirm proper fitting parameters and excellent agreement. The high-energy state at 2.5282 eV with a 2.1 ns PL decay time is assigned as the exciton emission pathway (blue). The low-energy state at 2.5119 eV with a 4.1 ns PL decay time pertains to the thermally activated emission pathway that is causing PL line width broadening at room temperature (red). The low-energy thermally activated emission pathway has a longer decay time than the exciton emission, verifying that the thermally activated alternate emission pathway is the sole contributor to longer PL decay times. In comparison, the 15 K spectrum in Figure 6b shows the disappearance of the thermally activated emission pathway (red fit) and the narrowing of the PL line width. The gradual disappearance of this phonon mode is observed at 130 and 170 K in Figure S6. As the thermal energy decreases, it is expected that phonon-assisted recombination would decrease as well. There is an additional fast component, 0.5 ns, for the PL monitored at approximately 2.52 eV (purple). Due to its energy and decay dynamics being comparable to those found in previous literature, this fast process may be attributed to biexciton Auger recombination. S0-52

At room temperature, the energy difference between the discrete states is 16.3 meV (131.5 cm⁻¹). At 15 K, the lowenergy tailing component decreases in intensity, and the exciton-phonon coupling mode diminishes. The energy difference that appears at room temperature suggests the formation of a thermally activated vibrational mode in agreement with the LO phonon energy (20 meV) calculated in Figure S7. The energy difference is in excellent agreement with previous reports that calculated LO phonon to be 16.5 meV. ^{9,53} The 131.5 cm⁻¹ vibrational mode is correlated to the transverse and LO phonon modes due to Pb-Br stretching vibrations in the octahedra.²⁸ A theoretical Raman study of lead-based perovskite single crystals identifies these optical phonon modes as the asymmetric (127 cm⁻¹) and symmetric (147 cm⁻¹) bending modes of the Pb-Br octahedra.²⁴ However, these modes are typically observed in PQDs with orthorhombic crystal symmetry, related to octahedral tilting, at low temperatures.²³ The evidence of the phonon-assisted emission pathway in the cubic structure suggests that the cubic polymorphs also experience vibrational distortions of the PbBr₆ octahedra and induce PL line width broadening at room temperature. The phonon-assisted emission also indicates the presence of intrinsic shallow trap state recombination that can be accessed only with phonon mediation.

The decrease in population of the alternate emission pathway and the long decay time (4.1 ns) indicate the presence of thermally activated shallow traps. Shallow trap states, unlike deep trap states, exist in high-quality nanocrystals. A high density of shallow traps accompanied by low phonon energies can lead to long carrier lifetimes. Kirchartz et al. conducted an analysis of the Huang—Rhys factor as a function of trap depth and found that systems with low phonon energies (minimum 16.5 meV) may lead to a strong dependence of recombination rates on trap depth. At room temperature, thermal energy accompanies the photoexcited electron and increases the likelihood of a vibrationally activated shallow trap state to facilitate phonon-assisted recombination. At low temperature, phonons are minimized due to a decrease in octahedral distortions that arise from vibrations.

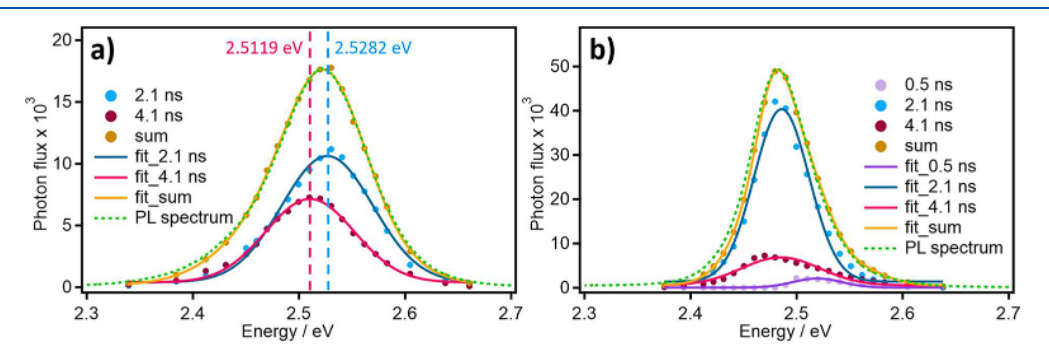


Figure 6. Energy-dependent time-resolved PL spectra at (a) 260 and (b) 15 K. Tetradecane PQD suspensions are frozen from 15 to 260 K to ensure QD aggregation is minimized. PL and TRPL measurements were conducted under the same conditions as in Figure 3a.

In summary, we demonstrated that PQD cubic phase still exhibits inhomogeneous PL line width broadening and longer PL lifetimes due to thermally activated phonon coupling to the exciton. This exciton-phonon coupling can be explained by PbBr₆ octahedral tilting that occurs at room temperature and pertains to the LO phonon energy (16.3 meV). The low LO phonon energy and long decay time (4.1 ns) for the phononassisted emission indicate the presence of thermally activated shallow traps. At 15 K, the phonon-assisted radiative recombination pathway is largely mitigated, as manifested by pure excitonic emission with minimal phonon-assisted emission. This suggests that the PbBr₆ octahedral distortions are minimized, and octahedral symmetry of the cubic phase is locked. Although the cubic phase PQDs are stabilized over a broad range of temperatures (15–300 K), they still experience some octahedral distortions related to lattice vibrations at room temperature. These distortions at room temperature confirm that the cubic phase polymorphous networks are thermally induced. Understanding the exciton-phonon coupling is an important step toward the rational design of high-performing, color pure optical emitters for photonics applications including solid-state lighting.

■ EXPERIMENTAL METHODS

Materials. Cesium carbonate (99.99%, Sigma-Aldrich), lead bromide (99.99%, Alfa Aezar), octadecene (90%, Sigma-Aldrich), oleic acid (90% tech grade, Sigma-Aldrich), and 70% tech grade oleylamine (Sigma-Aldrich). 70% tech grade oleylamine was purified using purification method by Baranov et al.⁵⁴

Preparation of Cs-oleate Precursor. A 0.40 g portion of Cs_2CO_3 was loaded into a 50 mL three-neck flask along with 18 mL of octadecene (ODE), 90%, and 2.5 mL of oleic acid (OA), 90%. Cs_2CO_3 is hygroscopic and was stored and weighed out in a N_2 glovebox. This solution was dried under vacuum for 1 h at 120 °C. The flask was then purged with N_2 and heated to 150 °C until all Cs_2CO_3 was reacted with oleic acid (about 5–10 min). The final solution is clear and translucent with a yellow tint when heated above 100 °C.

Since Cs-oleate precipitates out of the ODE at room temperature, it was preheated to 115 °C before injection.

Synthesis of CsPbBr₃ Perovskite Quantum Dots. A 0.188 mmol portion (0.069 g) of PbBr₂ was loaded into a 25 mL 3-neck round-bottom flask with 5.0 mL of the ODE. The solution was dried under vacuum with stirring for 1 h (ramp up to 120 °C in 30 min (4 °C/min)). The flask was then purged with N₂ and 0.5 mL dried oleylamine (OAm) and 0.50 mL dried oleic acid (OA) where injected at 120 °C. After complete solubilization of PbBr₂ salt, the precursor solution was heated to 170 °C. Cs-oleate precursor was heated to 115 °C for clear yellow solution. 0.40 mL (0.125M) of hot Cs-oleate was swiftly injected into PbBr₂ solution and reacted for 1 min with stirring (1000 rpm). Afterward, the reaction was immediately cooled in an ice water bath.

The crude solution was transferred into a 15 mL polypropylene centrifuge tube and centrifuged at 10,000 rpm for 3 min. The supernatant was discarded, and the resulting pellet was redispersed in 600 μ L of tetradecane by shaking (supernatant should luminescence blue under UV light, indicating formation of smaller particles). The suspension was then centrifuged at 10,000 rpm for 3 min. The quantum dots within the supernatant were kept, and the pellet was discarded. The resulting supernatant was diluted with 3.6 mL

of tetradecane. The PL spectral profiles of 260 and 15 K were collected to ensure the sample was solidified for both measurements since 260 K is well below the freezing point temperature of tetradecane.

PLQY Methods. Relative PLQY was measured via a custom-built PLQY system equipped with a UV white light source, a 405 nm LED light source, and a spectrometer to sequentially observe the transmission and emission spectra of the nanoparticles. We calculated PLQY using eq 1 and compared it against a perylene dye standard.

$$\Phi_{X} = \Phi_{ST} \left(\frac{Grad_{X}}{Grad_{ST}} \right) \left(\frac{{\eta_{X}}^{2}}{{\eta_{ST}}^{2}} \right)$$
(1)

HR-TEM. High-resolution transmission electron microscopy (HR-TEM) was performed on an FEI UT Tecnai microscope operated at 200 kV acceleration voltage. Diameter measurements were taken directly from the electron microscopy images using ImageJ software. For each sample, 150 PQD lengths were used to calculate the average diameter of 9 ± 1 nm.

XRD. X-ray diffraction (XRD) was performed on a Rigaku diffractometer operated in BB mode (10 mm) with a $\kappa\beta$ filter. Diffraction patterns were analyzed by using SmartLab Studio II software.

Steady-State PL Methods. Steady-state PL measurements were taken using a 405 nm pulsed wave laser (\sim 0.9 μ W average power) for direct comparison to the TRPL. The Andor Technology Step and Glue function was utilized to collect the entirety of the high-resolution spectrum with an 1800 lines/mm grating and 1000 μ m slit width.

PL trend measurements were taken by using a 405 nm continuous wave source (7 mW), a 150 lines/mm grating, and 1000 μ m slit width. All PL measurements were taken and analyzed using Andor Software:Solis. Each measurement was automated in LabView and held for 15 min to ensure thermal equilibrium.

There is an offset in room-temperature trend values for peak maximum (Figure 3b, 2.50 eV) in comparison to the previous PL measurements (Figure 3a, 2.52 meV), which used a higher resolution grating; however, the trend is unaffected by this parameter. The origin of inconsistency is dependent on instrumental calibration such as grating resolution and slit width.

Time-Resolved PL Methods (Energy-Dependent TRPL Methods). TRPL measurements were measured using time-correlated single-photon counting (Micron photon device) and analyzed using Timeharp 260 software. The measurements were taken using a 405 nm pulsed wave source (\sim 0.9 μ W average power), a 1800 lines/mm grating, 0.2 ns resolutions, and a 1000 μ m input slit width/100 μ m output slit width. Slit widths were calibrated to ensure proper overlay between steady-state and time-resolved PL spectra. Calibrations are depicted in Figure S9. Illumination studies were executed to ensure samples were stable under continuous and pulsed illumination for a 16 h period.

ASSOCIATED CONTENT

Supporting Information

The Supporting Information is available free of charge at https://pubs.acs.org/doi/10.1021/acs.jpclett.3c02568.

PQD concentration and power-dependent measurements, PQD PL QY stability measurements, Raman spectra of PQDs, accompanying PL/TRPL temperature

data for 130 and 170 K, fwhm fitting model equation, and output slit width and grating resolution calibration (PDF)

AUTHOR INFORMATION

Corresponding Authors

Jason K. Cooper — Chemical Science Division, Liquid Sunlight Alliance (LiSA), Lawrence Berkeley National Laboratory, Berkeley, California 94720, United States; oocid.org/ 0000-0002-7953-4229; Email: jkcooper@lbl.gov

Jin Z. Zhang — Department of Chemistry and Biochemistry, University of California, Santa Cruz, California 95064, United States; o orcid.org/0000-0003-3437-912X; Email: zhang@ucsc.edu

Authors

Vivien L. Cherrette – Department of Chemistry and Biochemistry, University of California, Santa Cruz, California 95064, United States

Finn Babbe — Chemical Science Division, Liquid Sunlight Alliance (LiSA), Lawrence Berkeley National Laboratory, Berkeley, California 94720, United States; orcid.org/ 0000-0002-9131-638X

Complete contact information is available at: https://pubs.acs.org/10.1021/acs.jpclett.3c02568

Notes

The authors declare no competing financial interest.

ACKNOWLEDGMENTS

This material is based upon work supported by the U.S. Department of Energy, Office of Science, Office of Workforce Development for Teachers and Scientists, Office of Science Graduate Student Research (SCGSR) program. The SCGSR program is administered by the Oak Ridge Institute for Science and Education (ORISE) for the DOE. ORISE is managed by ORAU under contract number DE-SC0014664. All opinions expressed in this paper are the author's and do not necessarily reflect the policies and views of DOE, ORAU, or ORISE. V.L.C. is grateful to the Liquid Sunlight Alliance (LiSA) at Lawrence Berkeley National Laboratory (LBNL) for the use of their B30 facilities. V.L.C. acknowledges the support in data analysis from Sayantani Ghosh, UC Merced, and Jeremy Barnett, UCSC. F.B. and J.K.C. acknowledge support from the U.S. Department of Energy, Office of Science, Office of Basic Energy Sciences, Fuels from Sunlight Hub under Award Number DE-SC0021266. Zhang lab at UCSC is grateful to the US NSF for financial support (CHE-1904547 and CHE-2203633). We would like to acknowledge the Molecular Foundry National Center of Electron Microscopy (NCEM) at LBNL for the HR-TEM.

REFERENCES

- (1) Akkerman, Q. A.; Rainò, G.; Kovalenko, M. V.; Manna, L. Genesis, Challenges and Opportunities for Colloidal Lead Halide Perovskite Nanocrystals. *Nat. Mater.* **2018**, *17* (5), 394–405.
- (2) Dey, A.; Ye, J.; De, A.; Debroye, E.; Ha, S. K.; Bladt, E.; Kshirsagar, A. S.; Wang, Z.; Yin, J.; Wang, Y.; Quan, L. N.; Yan, F.; Gao, M.; Li, X.; Shamsi, J.; Debnath, T.; Cao, M.; Scheel, M. A.; Kumar, S.; Steele, J. A.; Gerhard, M.; Chouhan, L.; Xu, K.; Wu, X.; Li, Y.; Zhang, Y.; Dutta, A.; Han, C.; Vincon, I.; Rogach, A. L.; Nag, A.; Samanta, A.; Korgel, B. A.; Shih, C.-J.; Gamelin, D. R.; Son, D. H.; Zeng, H.; Zhong, H.; Sun, H.; Demir, H. V.; Scheblykin, I. G.; Mora-

- Seró, I.; Stolarczyk, J. K.; Zhang, J. Z.; Feldmann, J.; Hofkens, J.; Luther, J. M.; Pérez-Prieto, J.; Li, L.; Manna, L.; Bodnarchuk, M. I.; Kovalenko, M. V.; Roeffaers, M. B. J.; Pradhan, N.; Mohammed, O. F.; Bakr, O. M.; Yang, P.; Müller-Buschbaum, P.; Kamat, P. V.; Bao, Q.; Zhang, Q.; Krahne, R.; Galian, R. E.; Stranks, S. D.; Bals, S.; Biju, V.; Tisdale, W. A.; Yan, Y.; Hoye, R. L. Z.; Polavarapu, L. State of the Art and Prospects for Halide Perovskite Nanocrystals. *ACS Nano* **2021**, *15* (7), 10775–10981.
- (3) Zhang, Q.; Shang, Q.; Su, R.; Do, T. T. H.; Xiong, Q. Halide Perovskite Semiconductor Lasers: Materials, Cavity Design, and Low Threshold. *Nano Lett.* **2021**, *21* (5), 1903–1914.
- (4) Liu, M.; Grandhi, G. K.; Matta, S.; Mokurala, K.; Litvin, A.; Russo, S.; Vivo, P. Halide Perovskite Nanocrystal Emitters. *Adv. Photonics Res.* **2021**, *2* (3), 2000118.
- (5) Wang, Y.; Li, X.; Song, J.; Xiao, L.; Zeng, H.; Sun, H. All-Inorganic Colloidal Perovskite Quantum Dots: A New Class of Lasing Materials with Favorable Characteristics. *Adv. Mater.* **2015**, *27* (44), 7101–7108.
- (6) Rainò, G.; Yazdani, N.; Boehme, S. C.; Kober-Czerny, M.; Zhu, C.; Krieg, F.; Rossell, M. D.; Erni, R.; Wood, V.; Infante, I.; Kovalenko, M. V. Ultra-Narrow Room-Temperature Emission from Single CsPbBr3 Perovskite Quantum Dots. *Nat. Commun.* **2022**, *13* (1), 2587.
- (7) Janke, E. M.; Williams, N. E.; She, C.; Zherebetskyy, D.; Hudson, M. H.; Wang, L.; Gosztola, D. J.; Schaller, R. D.; Lee, B.; Sun, C.; Engel, G. S.; Talapin, D. V. Origin of Broad Emission Spectra in InP Quantum Dots: Contributions from Structural and Electronic Disorder. J. Am. Chem. Soc. 2018, 140 (46), 15791–15803.
- (8) Cho, E.; Kim, T.; Choi, S.; Jang, H.; Min, K.; Jang, E. Optical Characteristics of the Surface Defects in InP Colloidal Quantum Dots for Highly Efficient Light-Emitting Applications. ACS Appl. Nano Mater. 2018, 1 (12), 7106–7114.
- (9) Kirchartz, T.; Markvart, T.; Rau, U.; Egger, D. A. Impact of Small Phonon Energies on the Charge-Carrier Lifetimes in Metal-Halide Perovskites. *J. Phys. Chem. Lett.* **2018**, 9 (5), 939–946.
- (10) Protesescu, L.; Yakunin, S.; Bodnarchuk, M. I.; Krieg, F.; Caputo, R.; Hendon, C. H.; Yang, R. X.; Walsh, A.; Kovalenko, M. V. Nanocrystals of Cesium Lead Halide Perovskites (CsPbX 3, X = Cl, Br, and I): Novel Optoelectronic Materials Showing Bright Emission with Wide Color Gamut. *Nano Lett.* **2015**, *15* (6), 3692–3696.
- (11) ten Brinck, S.; Zaccaria, F.; Infante, I. Defects in Lead Halide Perovskite Nanocrystals: Analogies and (Many) Differences with the Bulk. ACS Energy Lett. 2019, 4 (11), 2739–2747.
- (12) Li, J.; Yuan, X.; Jing, P.; Li, J.; Wei, M.; Hua, J.; Zhao, J.; Tian, L. Temperature-Dependent Photoluminescence of Inorganic Perovskite Nanocrystal Films. *RSC Adv.* **2016**, *6* (82), 78311–78316.
- (13) Lee, S. M.; Moon, C. J.; Lim, H.; Lee, Y.; Choi, M. Y.; Bang, J. Temperature-Dependent Photoluminescence of Cesium Lead Halide Perovskite Quantum Dots: Splitting of the Photoluminescence Peaks of CsPbBr ₃ and CsPb(Br/I) ₃ Quantum Dots at Low Temperature. *J. Phys. Chem. C* **2017**, *121* (46), 26054–26062.
- (14) Zhao, X.-G.; Dalpian, G. M.; Wang, Z.; Zunger, A. Polymorphous Nature of Cubic Halide Perovskites. *Phys. Rev. B* **2020**, *101* (15), 155137.
- (15) Swarnkar, A.; Marshall, A. R.; Sanehira, E. M.; Chernomordik, B. D.; Moore, D. T.; Christians, J. A.; Chakrabarti, T.; Luther, J. M. Quantum Dot-Induced Phase Stabilization of α -CsPbI $_3$ Perovskite for High-Efficiency Photovoltaics. *Science* **2016**, 354 (6308), 92–95.
- (16) Sercel, P. C.; Lyons, J. L.; Wickramaratne, D.; Vaxenburg, R.; Bernstein, N.; Efros, A. L. Exciton Fine Structure in Perovskite Nanocrystals. *Nano Lett.* **2019**, *19* (6), 4068–4077.
- (17) Cottingham, P.; Brutchey, R. L. On the Crystal Structure of Colloidally Prepared CsPbBr ₃ Quantum Dots. *Chem. Commun.* **2016**, 52 (30), 5246–5249.
- (18) Whitcher, T. J.; Gomes, L. C.; Zhao, D.; Bosman, M.; Chi, X.; Wang, Y.; Carvalho, A.; Hui, H. K.; Chang, Q.; Breese, M. B. H.; Castro Neto, A. H.; Wee, A. T. S.; Sun, H. D.; Chia, E. E. M.; Rusydi, A. Dual Phases of Crystalline and Electronic Structures in the

- Nanocrystalline Perovskite CsPbBr3. NPG Asia Mater. 2019, 11 (1), 70.
- (19) Fu, Y.; Jiang, X.; Li, X.; Traore, B.; Spanopoulos, I.; Katan, C.; Even, J.; Kanatzidis, M. G.; Harel, E. Cation Engineering in Two-Dimensional Ruddlesden-Popper Lead Iodide Perovskites with Mixed Large A-Site Cations in the Cages. *J. Am. Chem. Soc.* **2020**, *142* (8), 4008–4021.
- (20) Prasanna, R.; Gold-Parker, A.; Leijtens, T.; Conings, B.; Babayigit, A.; Boyen, H.-G.; Toney, M. F.; McGehee, M. D. Band Gap Tuning via Lattice Contraction and Octahedral Tilting in Perovskite Materials for Photovoltaics. *J. Am. Chem. Soc.* **2017**, *139* (32), 11117–11124.
- (21) Fabini, D. H.; Laurita, G.; Bechtel, J. S.; Stoumpos, C. C.; Evans, H. A.; Kontos, A. G.; Raptis, Y. S.; Falaras, P.; Van der Ven, A.; Kanatzidis, M. G.; Seshadri, R. Dynamic Stereochemical Activity of the Sn ²⁺ Lone Pair in Perovskite CsSnBr ₃. *J. Am. Chem. Soc.* **2016**, 138 (36), 11820–11832.
- (22) Iaru, C. M.; Geuchies, J. J.; Koenraad, P. M.; Vanmaekelbergh, D.; Silov, A. Yu. Strong Carrier-Phonon Coupling in Lead Halide Perovskite Nanocrystals. *ACS Nano* **2017**, *11* (11), 11024–11030.
- (23) Huang, X.; Li, X.; Tao, Y.; Guo, S.; Gu, J.; Hong, H.; Yao, Y.; Guan, Y.; Gao, Y.; Li, C.; Lü, X.; Fu, Y. Understanding Electron-Phonon Interactions in 3D Lead Halide Perovskites from the Stereochemical Expression of 6s ² Lone Pairs. *J. Am. Chem. Soc.* **2022**, 144 (27), 12247–12260.
- (24) Naqvi, F. H.; Ko, J.-H.; Kim, T. H.; Ahn, C. W.; Hwang, Y.; Sheraz, M.; Kim, S. A-Site Cation Effect on Optical Phonon Modes and Thermal Stability in Lead-Based Perovskite Bromide Single Crystals Using Raman Spectroscopy. *J. Korean Phys. Soc.* **2022**, *81* (3), 230–240.
- (25) Sarang, S.; Bonabi Naghadeh, S.; Luo, B.; Kumar, P.; Betady, E.; Tung, V.; Scheibner, M.; Zhang, J. Z.; Ghosh, S. Stabilization of the Cubic Crystalline Phase in Organometal Halide Perovskite Quantum Dots via Surface Energy Manipulation. *J. Phys. Chem. Lett.* **2017**, *8* (21), 5378–5384.
- (26) Wright, A. D.; Verdi, C.; Milot, R. L.; Eperon, G. E.; Pérez-Osorio, M. A.; Snaith, H. J.; Giustino, F.; Johnston, M. B.; Herz, L. M. Electron-Phonon Coupling in Hybrid Lead Halide Perovskites. *Nat. Commun.* **2016**, *7* (1), 11755.
- (27) Lao, X.; Yang, Z.; Su, Z.; Bao, Y.; Zhang, J.; Wang, X.; Cui, X.; Wang, M.; Yao, X.; Xu, S. Anomalous Temperature-Dependent Exciton-Phonon Coupling in Cesium Lead Bromide Perovskite Nanosheets. J. Phys. Chem. C 2019, 123 (8), 5128–5135.
- (28) Zhao, Z.; Zhong, M.; Zhou, W.; Peng, Y.; Yin, Y.; Tang, D.; Zou, B. Simultaneous Triplet Exciton-Phonon and Exciton-Photon Photoluminescence in the Individual Weak Confinement CsPbBr ₃ Micro/Nanowires. *J. Phys. Chem. C* **2019**, *123* (41), 25349–25358.
- (29) Hirotsu, S.; Harada, J.; Iizumi, M.; Gesi, K. Structural Phase Transitions in CsPbBr ₃. *J. Phys. Soc. Jpn.* **1974**, 37 (5), 1393–1398.
- (30) Mannino, G.; Deretzis, İ.; Smecca, E.; La Magna, A.; Alberti, A.; Ceratti, D.; Cahen, D. Temperature-Dependent Optical Band Gap in CsPbBr ₃, MAPbBr ₃, and FAPbBr ₃ Single Crystals. *J. Phys. Chem. Lett.* **2020**, *11* (7), 2490–2496.
- (31) He, Y.; Matei, L.; Jung, H. J.; McCall, K. M.; Chen, M.; Stoumpos, C. C.; Liu, Z.; Peters, J. A.; Chung, D. Y.; Wessels, B. W.; Wasielewski, M. R.; Dravid, V. P.; Burger, A.; Kanatzidis, M. G. High Spectral Resolution of Gamma-Rays at Room Temperature by Perovskite CsPbBr3 Single Crystals. *Nat. Commun.* **2018**, *9* (1), 1609.
- (32) Diroll, B. T.; Zhou, H.; Schaller, R. D. Low-Temperature Absorption, Photoluminescence, and Lifetime of CsPbX ₃ (X = Cl, Br, I) Nanocrystals. *Adv. Funct. Mater.* **2018**, 28 (30), 1800945.
- (33) Brennan, M. C.; Kuno, M.; Rouvimov, S. Crystal Structure of Individual CsPbBr ₃ Perovskite Nanocubes. *Inorg. Chem.* **2019**, *58* (2), 1555–1560.
- (34) Zhang, Q.; Su, R.; Liu, X.; Xing, J.; Sum, T. C.; Xiong, Q. High-Quality Whispering-Gallery-Mode Lasing from Cesium Lead Halide Perovskite Nanoplatelets. *Adv. Funct. Mater.* **2016**, 26 (34), 6238–6245.

- (35) Qaid, S. M. H.; Ghaithan, H. M.; Al-Asbahi, B. A.; Aldwayyan, A. S. Achieving Optical Gain of the CsPbBr ₃ Perovskite Quantum Dots and Influence of the Variable Stripe Length Method. *ACS Omega* **2021**, *6* (8), 5297–5309.
- (36) Giovanni, D.; Righetto, M.; Zhang, Q.; Lim, J. W. M.; Ramesh, S.; Sum, T. C. Origins of the Long-Range Exciton Diffusion in Perovskite Nanocrystal Films: Photon Recycling vs Exciton Hopping. *Light Sci. Appl.* **2021**, *10* (1), 2.
- (37) Li, J.; Yuan, X.; Jing, P.; Li, J.; Wei, M.; Hua, J.; Zhao, J.; Tian, L. Temperature-Dependent Photoluminescence of Inorganic Perovskite Nanocrystal Films. *RSC Adv.* **2016**, *6* (82), 78311–78316.
- (38) Aceves, R.; Babin, V.; Flores, M. B.; Fabeni, P.; Maaroos, A.; Nikl, M.; Nitsch, K.; Pazzi, G. P.; Salas, R. P.; Sildos, I.; Zazubovich, N.; Zazubovich, S. Spectroscopy of CsPbBr3 Quantum Dots in CsBr:Pb Crystals. *J. Lumin.* **2001**, *93* (1), 27–41.
- (39) Nikl, M.; Nitsch, K.; Mihóková, E.; Polák, K.; Fabeni, P.; Pazzi, G. P.; Gurioli, M.; Santucci, S.; Phani, R.; Scacco, A.; Somma, F. Luminescence of CsPbBr3-like Quantum Dots in CsBr Single Crystals. *Phys. E Low-Dimens. Syst. Nanostructures* **1999**, 4 (4), 323–331.
- (40) Kim, Y.-H.; Kim, S.; Kakekhani, A.; Park, J.; Park, J.; Lee, Y.-H.; Xu, H.; Nagane, S.; Wexler, R. B.; Kim, D.-H.; Jo, S. H.; Martínez-Sarti, L.; Tan, P.; Sadhanala, A.; Park, G.-S.; Kim, Y.-W.; Hu, B.; Bolink, H. J.; Yoo, S.; Friend, R. H.; Rappe, A. M.; Lee, T.-W. Comprehensive Defect Suppression in Perovskite Nanocrystals for High-Efficiency Light-Emitting Diodes. *Nat. Photonics* **2021**, *15* (2), 148–155.
- (41) Utzat, H.; Sun, W.; Kaplan, A. E. K.; Krieg, F.; Ginterseder, M.; Spokoyny, B.; Klein, N. D.; Shulenberger, K. E.; Perkinson, C. F.; Kovalenko, M. V.; Bawendi, M. G. Coherent Single-Photon Emission from Colloidal Lead Halide Perovskite Quantum Dots. *Science* **2019**, 363 (6431), 1068–1072.
- (42) Momma, K.; Izumi, F. VESTA, 2011.
- (43) Zhang, D.; Eaton, S. W.; Yu, Y.; Dou, L.; Yang, P. Solution-Phase Synthesis of Cesium Lead Halide Perovskite Nanowires. *J. Am. Chem. Soc.* **2015**, *137* (29), 9230–9233.
- (44) Ledinsky, M.; Schönfeldová, T.; Holovský, J.; Aydin, E.; Hájková, Z.; Landová, L.; Neyková, N.; Fejfar, A.; De Wolf, S. Temperature Dependence of the Urbach Energy in Lead Iodide Perovskites. J. Phys. Chem. Lett. 2019, 10 (6), 1368–1373.
- (45) Klingshirn, C. F. Semiconductor Optics; Graduate Texts in Physics; Springer: Berlin, 2012.
- (46) Xie, Y.; Peng, B.; Bravić, I.; Yu, Y.; Dong, Y.; Liang, R.; Ou, Q.; Monserrat, B.; Zhang, S. Highly Efficient Blue-Emitting CsPbBr ₃ Perovskite Nanocrystals through Neodymium Doping. *Adv. Sci.* **2020**, 7 (20), 2001698.
- (47) Thomson, S. Application Note: Observing Phase Transitions in a Halide Perovskite Using Temperature Dependent Photoluminescence Spectroscopy; Edinburgh Instruments; 2018. https://www.edinst.com/wp-content/uploads/2018/05/AN45_Phase-Transitions_Halide-Perovskites.pdf. (accessed 2022-09-14).
- (48) Lee, S. M.; Moon, C. J.; Lim, H.; Lee, Y.; Choi, M. Y.; Bang, J. Temperature-Dependent Photoluminescence of Cesium Lead Halide Perovskite Quantum Dots: Splitting of the Photoluminescence Peaks of CsPbBr 3 and CsPb(Br/I) 3 Quantum Dots at Low Temperature. *J. Phys. Chem. C* **2017**, *121* (46), 26054–26062.
- (49) Chen, H.; Guo, A.; Zhu, J.; Cheng, L.; Wang, Q. Tunable Photoluminescence of CsPbBr3 Perovskite Quantum Dots for Their Physical Research. *Appl. Surf. Sci.* **2019**, *465*, 656–664.
- (50) Makarov, N. S.; Guo, S.; Isaienko, O.; Liu, W.; Robel, I.; Klimov, V. I. Spectral and Dynamical Properties of Single Excitons, Biexcitons, and Trions in Cesium-Lead-Halide Perovskite Quantum Dots. *Nano Lett.* **2016**, *16* (4), 2349–2362.
- (51) Li, X.; Wu, Y.; Steel, D.; Gammon, D.; Stievater, T. H.; Katzer, D. S.; Park, D.; Piermarocchi, C.; Sham, L. J. An All-Optical Quantum Gate in a Semiconductor Quantum Dot. *Science* **2003**, *301* (5634), 809–811.
- (52) Zhu, C.; Nguyen, T.; Boehme, S. C.; Moskalenko, A.; Dirin, D. N.; Bodnarchuk, M. I.; Katan, C.; Even, J.; Rainò, G.; Kovalenko, M.

- V. Many-Body Correlations and Exciton Complexes in CsPbBr ₃ Quantum Dots. *Adv. Mater.* **2023**, *35* (9), 2208354.
- (53) Sendner, M.; Nayak, P. K.; Egger, D. A.; Beck, S.; Müller, C.; Epding, B.; Kowalsky, W.; Kronik, L.; Snaith, H. J.; Pucci, A.; Lovrinčić, R. Optical Phonons in Methylammonium Lead Halide Perovskites and Implications for Charge Transport. *Mater. Horiz.* **2016**, *3* (6), 613–620.
- (54) Baranov, D.; Lynch, M. J.; Curtis, A. C.; Carollo, A. R.; Douglass, C. R.; Mateo-Tejada, A. M.; Jonas, D. M. Purification of Oleylamine for Materials Synthesis and Spectroscopic Diagnostics for *Trans* Isomers. *Chem. Mater.* **2019**, *31* (4), 1223–1230.